5 FEL Parameters and Performance

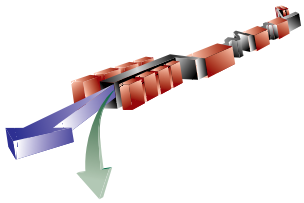

TECHNICAL SYNOPSIS

The FEL parameter optimization and performance characterizations that are described in Chapter 5 are based on three-dimensional theory and computer models. The investigation led to a selection of the best parameters and to a study of the sensitivity to changes in values of accelerator components and beam characteristics and to unavoidable imperfections in the settings of the beam characteristics, magnetic and mechanical components and electron beam monitoring. The focusing of the electron beam plays an important role in the production of the FEL radiation. The LCLS undulator optics has been optimized in terms of its focusing lattice and strength. The electron optics consists of FODO cells; with cell lengths between 7.3 m and 7.5 m. Focusing is obtained by placing permanent magnet quadrupoles in the breaks between the undulator sections. The correction of the electron orbit is obtained by a small lateral displacement of the quadrupoles. Simulations indicate that the FEL radiation saturates at a length of ~90 m. The proposed LCLS undulator has a magnetic length of 121 m, since it is a requirement that the FEL operate in the saturation regime. This fact not only gives the maximum output power, but also reduces the pulse-to-pulse fluctuations of the radiation.

Complete simulations of the LCLS, starting from the photocathode, and continuing through injector, linac, and undulator are an important help for understanding all of these effects and their impact on LCLS operation. The simulations, reported in this chapter, include thermal, rf, and space charge effects in the injector system, and wakefields and CSR in the linac-compressor system. The results of the simulations, presented for two cases, i.e., 1 nC and 0.25 nC bunch charge, show that under idealized conditions the beam emittance is small, about 0.5 and 0.3 μm-rad, respectively. Even with this small beam emittance, the wakefield effects in the linac and compressors reduce the LCLS output power and produce a transverse displacement and frequency chirp along the bunch.

The possibility of changing (i.e., lowering) the output power was investigated. This may be desirable if the peak power on the sample is excessive and if required for experimental purposes. The reduction in power, by either reducing the electron current or by increasing the beam emittance, is accompanied by an increase in fluctuations of the output power due to fluctuations in the beam characteristics from pulse-to-pulse, since the FEL no longer operates in the saturation regime. For this reason, the best way to reduce the output power is by placing an FEL absorption cell in the path of the radiation, as discussed in Chapter 9.

During commissioning both the electron beam and the x-ray radiation will be intensively characterized. Special x-ray commissioning diagnostics will be used, as described in Chapter 9.

5.1 Introduction

The SASE process will produce pulses of coherent FEL x-ray radiation in the LCLS undulator with a harmonic spectrum that is adjustable over a large wavelength range. The operational wavelength is controlled by changing the energy of the electrons as described in **Chapter 4** (**Equation 4.1**). The LCLS linac is designed to accelerator electrons to a final energy that is adjustable within the operational range between 4.54 GeV and 14.35 GeV. The FEL wavelength is proportional to the inverse of the square of the electron energy. The electron energy can be changed between 4.54 GeV and 14.35 GeV. The low energy limit corresponds to a wavelength of 15 Å for the fundamental and 5 Å for the third harmonic. The high-energy limit corresponds to a wavelength of 1.5 Å for the fundamental and 0.5 Å for the third harmonic. In addition to the coherent FEL radiation harmonics there will be a continuous spectrum of ordinary, incoherent undulator radiation, although much more intense than from ordinary insertion devices due to the high energy of the electron beam and the great length of the undulator.

The undulator consists of 33 individual undulator segments that are separated from each other by about 20- to 40-cm-long breaks, to provide space for focusing, steering, diagnostics and vacuum components. The lengths of these breaks are designed so that the x-ray pulse and the electron beam slip with respect to each either by one or by two optical wavelengths, thus keeping the electrons in phase with the radiation. As described in **Chapter 8,** the first three breaks are individually adjusted to minimize the overall saturation length.

FEL theory predicts that the SASE process will saturate at about 90 m after the entrance to the undulator for the proposed baseline parameter set. This length includes the breaks between undulator segments. The tolerance budget for the undulator and the electron beam parameters has been set to limit the increase in saturation length to 1 field gain length, or about 10 m. The total length of the LCLS undulator is 121 m for operational contingency.

The basic FEL parameters of the LCLS are discussed in **Section 5.2**. The design of the focusing system is discussed in **Section 5.3**. Computer simulations are described in **Section 5.4.** Sources of gain reduction and resulting tolerances are discussed in **Section 5.5.** Electron beam tolerances are discussed in **Section 5.6. Section 5.7** discusses the temporal structure of the x-ray pulse. **Section 5.8** gives an overview of the LCLS Commissioning

5.2 The Basic LCLS FEL Design

5.2.1 Overview

The basic parameters used to describe the FEL process include, for the electron beam, electron energy, E, normalized emittance, ε_n, peak current, I_{pk}, and relative rms energy spread σ_E/E, and for the undulator, type, period, λ_U, gap, g, peak field, B_U, and average beta-function, $<\beta_{x,y}>$. From these parameters follow the undulator parameter, K, and the fundamental

wavelength FEL radiation wavelength, λ_r. The nominal values for these parameters are listed in **Table 5.2**, their choice is discussed in the following sections.

5.2.2 Slice Parameters

As described in **Chapter 4**, the FEL instability comes from an interaction between the bunch electrons and the electromagnetic wave that is generated by those electrons and that is traveling with the electrons. At a given point in the process, the interaction is local on the scale of the optical wavelength. Interactions between different parts of the bunch occur due to slippage, i.e. due to the fact the for every undulator period traveled by the radiation, the electron beam falls behind by one optical wavelength. Thus the electrons in a given wavelength section interact with the radiation generated by electrons traveling at locations further towards the head of the bunch. This interaction is therefore limited to electrons that are not further apart in the bunch than the total slippage distance, $L_{slip} = N_u \lambda_r$, that corresponds to the total passage of the electron beam through the undulator, where N_U is the total number of undulator periods. At a given position in the undulator during the exponential gain process, radiation that has been produced when the bunch was more than a power gain length before that position can practically be neglected compared to the more recently produced radiation amplitudes. The term cooperation length as the slippage length over one power gain length has been introduced to name the distance within the bunch over which there is strong interaction between bunch electrons through the electromagnetic radiation produced and acted upon by the bunch electrons. The FEL process is thus determined locally within a longitudinal slice of the electron bunch that has a thickness or length of the order of a cooperation length.

The FEL dynamics in one slice is not affected by the electron distribution in another slice if the two slices are significantly further apart than one cooperation length. If spatially separated slices have different electron energies they will just generate radiation of different wavelengths, the energy difference does not act as energy spread for the FEL process; only the energy distribution of the particles within a slice is relevant. Similar statements can be made for the emittances of the slices, the slices' relative transverse positions and their peak currents. Often, those parameters change along the electron bunch. If the bunch is much longer than the cooperation length, as is the case for the LCLS, it is important to distinguish between slice parameters and projected parameters. The projected parameters that are obtained after projecting the bunch to the same plane will give unrealistically pessimistic results when used to predict FEL performance. Reasonable performance predictions have to be done using projections over the width of a slice, only. The performance will be a function of the slice's position along the bunch. Whenever the terms emittance, energy spread and peak current are used in this report to characterize the FEL process they always stand for the terms slice emittance, slice energy spread and slice peak current. The terms projected emittance, projected energy spread, and average peak current are relevant because they name quantities that are more easily accessible to measurement and they affect the overall brightness of the x-ray pulses. For x-ray FELs such as the LCLS, the cooperation length is much shorter than the bunch length and presently too short to serve as a basis to measure slice parameters. Therefore the slice length if often increased to 5% to 10% of

the bunch length, a value that is more accessible to diagnostics. Applying tolerances set for cooperation lengths slices to 10% of bunch length slices is a conservative approach.

The term slice emittance is not only used to characterize the electron bunch inside the undulator but also through injector and linac. This makes sense because electromagnetic fields, produced by space charge, chamber impedance, and coherent synchrotron radiation, create a dependence of the transverse position of the beam centroid on its longitudinal position within the bunch while the local electron density remains unaffected. Computer simulations show that slice emittance is not strongly affected during the acceleration and bunch compression processes in the linac.

Also used in this report is the attribute, nominal, such as nominal projected emittance or nominal slice emittance, to specify goal values for the parameters.

5.2.3 Parameter Optimization

The design of the LCLS FEL configuration has been greatly simplify by the use of **Equations** (5.1) and (5.2) given in [1], a parameterization of the results of 3-D FEL theory developed between 1985 and 1995 [2] [3][4]:

$$\frac{L_{G,1D}}{L_G} = \frac{1}{1+\eta} \qquad \textbf{(5.1)}$$

where the parameter η is

$$\begin{aligned}\eta = \quad & a_1\eta_d^{a_2} + a_3\eta_\varepsilon^{a_4} + a_5\eta_\gamma^{a_6} + a_7\eta_\varepsilon^{a_8}\eta_\gamma^{a_9} + \\ & a_{10}\eta_d^{a_{11}}\eta_\gamma^{a_{12}} + a_{13}\eta_d^{a_{14}}\eta_\varepsilon^{a_{15}} + a_{16}\eta_d^{a_{17}}\eta_\varepsilon^{a_{18}}\eta_\gamma^{a_{19}}\end{aligned} \qquad \textbf{(5.2)}$$

L_G and $L_{G,1D}$ are the 3-D and 1-D gain length, respectively. The 19 fit coefficients, a_i, are shown in **Table 5.1**. The results of **Equations (5.1)** and **(5.2)** have been checked against 3-D simulation codes and are in excellent agreement.

Table 5.1 Coefficients for **Equation (5.2).**

a_1	a_2	a_3	a_4	a_5	a_6	a_7	a_8	a_9	a_{10}
0.45	0.57	0.55	1.6	3	2	0.35	2.9	2.4	51
a_{11}	a_{12}	a_{13}	a_{14}	a_{15}	a_{16}	a_{17}	a_{18}	a_{19}	
0.95	3	5.4	0.7	1.9	1140	2.2	2.9	3.2	

The scaling parameters express the deviation from the 1-D condition due to diffraction, η_d, emittance, η_ε and energy spread, η_γ:

$$\eta_d = \frac{L_{G,1D}}{2L_R}; \qquad \eta_\varepsilon = \frac{L_{G,1D}}{\beta_{x,y}}\frac{4\pi\ \varepsilon_n}{\lambda_r\ \gamma}; \qquad \eta_\gamma = \frac{4\pi\ \ L_{G,1D}}{\lambda_u}\frac{\sigma_E}{E}. \qquad \textbf{(5.3)}$$

Using the 1-D gain length

$$L_{G,1D} = \frac{\lambda_u}{4\pi\sqrt{3}\rho} \qquad \textbf{(5.4)}$$

and the total peak beam power

$$P_{b,pk} = I_{pk}\,\gamma\, mc^2/e \tag{5.5}$$

the peak power at saturation, P_{sat}, and the undulator length, L_{sat}, needed for saturation can be approximated by

$$P_{sat} \approx 1.6\rho\left(\frac{L_{G,1D}}{L_G}\right)^2 P_{b,pk} \tag{5.6}$$

and

$$L_{sat} \approx L_G \ln\left(\frac{P_{sat}}{\rho E e \Delta\omega}\right) \tag{5.7}$$

respectively. These equations use the FEL parameter, ρ, the bandwidth, $\Delta\omega$,

$$\Delta\omega = \frac{2\sigma_\gamma/\gamma}{\lambda_r}c \tag{5.8}$$

the speed of light, c, the electron charge, e, and the relative electron energy spread, σ_E/E. The parameter optimization is constraint by practical limits for a number of parameters, including the undulator gap, $g \geq 6$ mm, $E < 14.5$ GeV, $I_{pk} \leq 3400$ A, $\sigma_E / E \geq 0.0001$ and $L_u < 121$ m.

5.2.4 The Nominal Parameter Set

The LCLS is based on a planar hybrid undulator; this choice is discussed and justified in **Chapter 8**. Within the above constraints, the optimum operating parameters (**Table 5.2**) can be found using of **Equations** (5.1) and (5.2). A complete list of the LCLS parameters is given in **Appendix A**. These parameter tables are set up for the case that, except for the energy, the electron beam parameters are the same. Other parameter configurations are also available.

Table 5.2 Basic LCLS parameters at limits of operational wavelength range.

Parameter	Values		Unit
E	4.54	14.35	GeV
ε_n	1.2		μm-rad
I_{pk}	3400		A
RMS slice energy spread σ_E/E	0.025	0.008	%
Undulator Type	Planar Halbach HybridUndulator		
λ_u	0.03		m
g	6		mm
B_w	1.32		T
K	3.71		
$<\beta_{xy}>$	18	7.3	m
λ_r	15	1.5	Å

5.2.5 Working Points

This report uses sets of parameters. The term "working point" is used for nominal parameter sets at each wavelength. **Figure 5.1**, **Figure 5.2**, and **Figure 5.3** show the relation between the working points and the operational parameter space area at three different points within the operational range.

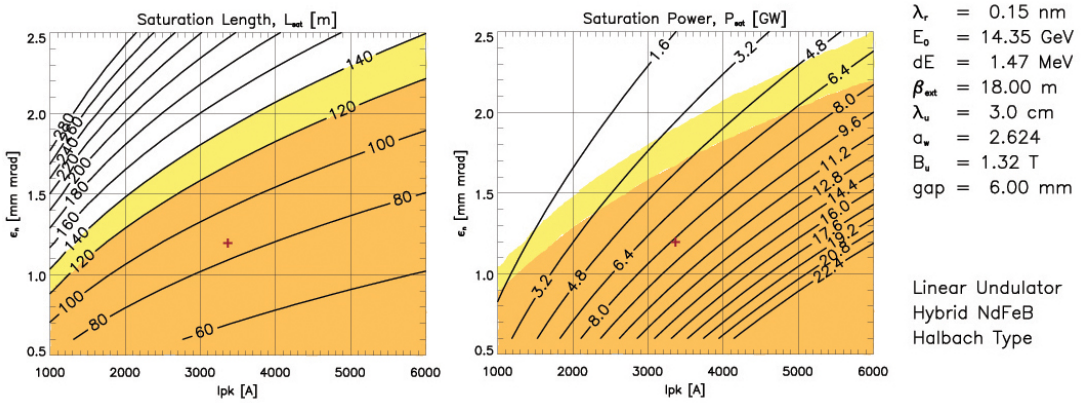

Figure 5.1 Contour diagram of the saturation length, L_{sat}, and saturation power, P_{sat}, as a function of normalized emittance, ε_n, and peak current, I_{pk} for at the 1.5 Å end of the LCLS operational range of the spectrum. The darker background color marks the parameter regime (peak current, normalized emittance) that will lead to saturation before the end of the 121-m long undulator. The parameter regime marked with lighter background shading will lead to saturation just after the end of undulator. The cross inside the dark background area marks the nominal working point. It is the center of an LCLS operational phase space volume. At the shortest wavelength, the nominal working point (ε_n = 1.2 μm-rad, I_{pk} = 3400 A) is expected to correspond to a saturation length of about 90 m, well before the end of the undulator. The change of saturation power over the operational phase space volume is about a factor 2, i.e., small compared to the total energy gained from the FEL process.

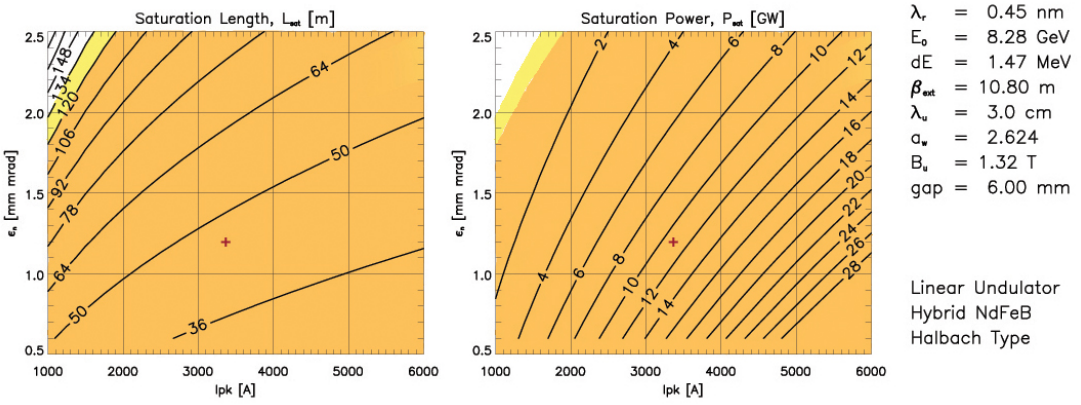

Figure 5.2 Contour diagram similar to **Figure 5.1** but at the longer wavelength of the 4.5 Å. The nominal operation point corresponds to a saturation length of less than 50 m, well before the center of the undulator. Much larger values of the normalized emittance and smaller values of the peak current will still keep the saturation point before the end of the undulator.

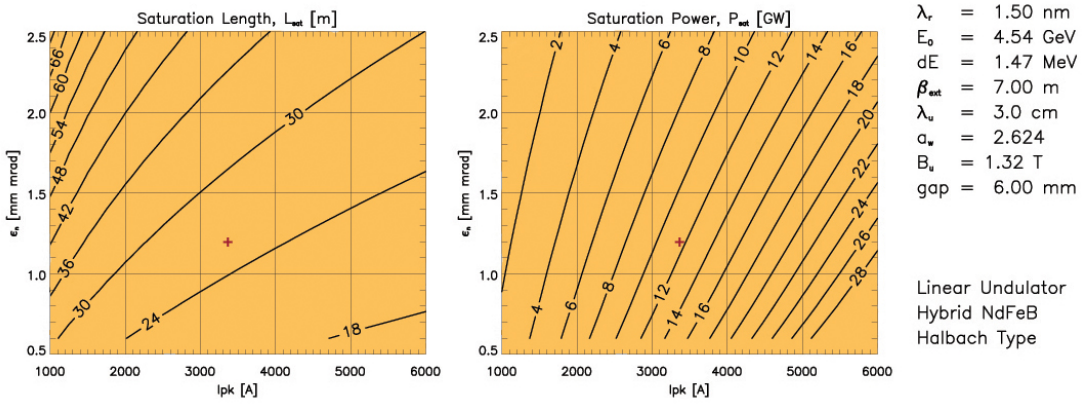

Figure 5.3 Contour diagram similar to **Figure 5.1** and **Figure 5.2** but at 15 Å, the long wavelength end of the operational range. The nominal operation point corresponds to a saturation length of about 25 m. At this long wavelength the FEL process will saturate before the end of the undulator for a large parameter area.

The figures also show how peak current can be traded against normalized emittance when keeping the saturation length constant.

5.3 Electron Beam Focusing Along the Undulator

The criteria that let to the selection of the average β-function, the quadrupole strength and the cell spacing were established by first determining the optimum of the average β-function, and, after that, the maximum tolerable amplitude of the modulation of the β-function.

5.3.1 Optimum Beam Size

As the electron beam is transported through the LCLS undulator, transverse focusing is applied to keep the beam size, $\sigma_{x,y}$, approximately constant at

$$\sigma_{x,y} = \sqrt{\beta_{x,y}\frac{\varepsilon_n}{\gamma}} \qquad \textbf{(5.9)}$$

In 1D FEL theory the beam size affects the FEL parameter, ρ, via the bunch electron density

$$n_e = \frac{I_{pk}}{2\pi\sigma_x\sigma_y ec}, \qquad \textbf{(5.10)}$$

resulting in a smaller gain length for a smaller beam size. 3-D effects, especially diffraction, will eventually lead to a decrease in FEL performance when the beam size becomes too small. **Figure 5.4** and **Figure 5.5** show relative FEL saturation power and saturation length as a function of the average β-function in the undulator for 1.5 Å and 15 Å.

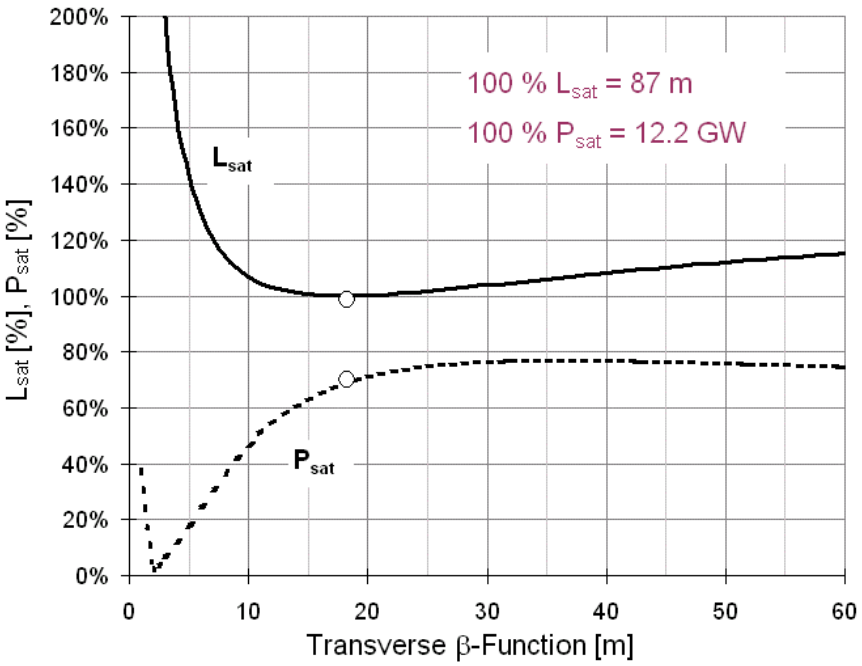

Figure 5.4 Power at saturation, P_{sat}, and saturation length, L_{sat}, as a percentage of 12.2 GW and 87 m, respectively, as a function of the average β-function at a radiation wavelength of 1.5 Å (14.35 GeV). The circles indicate the LCLS operating point.

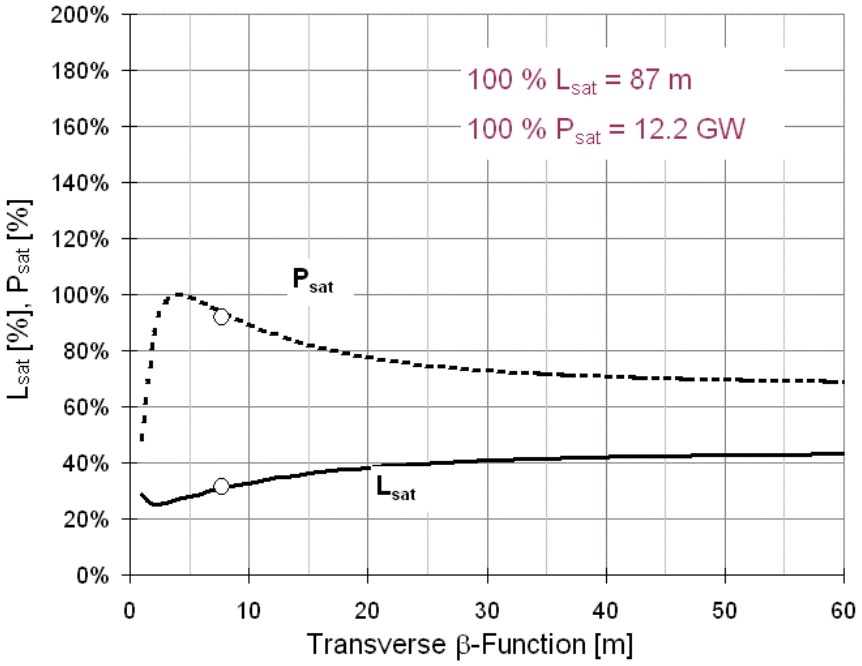

Figure 5.5 Power at saturation, P_{sat}, and saturation length, L_{sat}, as a percentage of 12.2 GW and 87 m, respectively, as a function of the average β-function at a radiation wavelength of 15 Å (4.54 GeV). The circles indicate the LCLS operating point.

At every energy in the proposed range between 4.54 GeV (15 Å) and 14.35 GeV (1.5 Å), the minimum saturation length and the maximum saturation power occur at different values of the average β-function. The saturation length at 15 GeV determines the length of the undulator. It is important at that energy to choose the β-function related to the minimum saturation length. This minimum occurs at a β-function of 18 m as is shown in **Figure 5.4**. This value was chosen for the 14.35 GeV end of the LCLS operations range.

The average β-function value at which minimum saturation length occurs decreases with energy to reach about 2.1 m at 4.54 GeV. The average β-function value at which maximum saturation power occurs decreases with energy as well and reaches about 5 m at 4.54 GeV. As discussed below, the β-function value chosen for the LCLS at 4.54 GeV is 7 m, which can be reached from the high-energy value with constant gradient focusing. At this β-function value the saturation power is close to its maximum, which is desirable. At 4.54 GeV saturation will occur during the first quarter of the undulator.

The following section discusses the need for and the choice of a quadrupole focusing lattice to generate the required average β-function.

5.3.2 Natural Undulator Focusing

In the ideal case the beam size along the undulator should be constant. Constant beam size focusing can, in principal, be achieved by using a modification to natural undulator focusing. It turns out that natural undulator focusing is too week to achieve the average β-function values required for the LCLS.

Natural focusing of a planar undulator exists in the plane perpendicular to the wiggle motion only (in this report, called x-plane, since the undulator, as shown in **Chapter 8**, has a vertical field). The focusing strength can be expressed by specifying the "natural" beta-function of the focusing system that is intrinsic to an undulator made of parallel poles

$$\beta_x^{nat} = \sqrt{2}\gamma / k_U K \qquad \textbf{(5.11)}$$

By appropriately shaping the pole faces, half the focusing can be directed into the wiggle plane. This type of constant focusing in both planes is called ted-pole focusing [10] or sextupole focusing.

$$\beta_{x,y}^{TP} = \sqrt{2}\beta_x^{nat} \qquad \textbf{(5.12)}$$

The amount of focusing that can be obtained this way is often smaller than required for optimum FEL performance, especially for high energy and short wavelength applications. For the LCLS the β-function from sextupole focusing alone would be 70 m at 14.35 GeV and 22 m at 4.54 GeV, which would increase the saturation length and thus the length of the undulator by 22% at 14.35 GeV.

5.3.3 Focusing Method (Lattice)

A focusing system stronger than that given by sextupole focusing can be obtained with external quadrupole fields. Possible lattice choices are two (FODO), three (Triplet), or more quadrupole magnets per unit cell. A FODO lattice was selected based on simplicity of design and on the cost-related desire to keep the number of magnets and associated instrumentation small. A Triplet lattice was studied and rejected because it establishes extremely tight alignment tolerances for the central quadrupole, which that could not be met.

Quadrupole focusing introduces an oscillation in the longitudinal phase of the electrons with respect to the ponderomotive potential well, while natural focusing maintains a constant phase [10]. This phase modulation could lead to de-trapping of particles and thus reduce FEL efficiency. Yu et al. [5], point out that such a reduction in gain can indeed occur for tapered wigglers, in which most of the output power is provided by trapped electrons, but that the same effect can actually be beneficial in the exponential gain regime. Here, the reduction of the dependence of the longitudinal velocity on betatron oscillation amplitudes in the case of alternating-gradient focusing tends to offset the effect of longitudinal velocity modulation.

The main betatron-oscillation of period, $2\pi/\beta$ is modulated due to the beam envelope modulations caused by the change in β-function along the quadrupole lattice. The period of these modulations is equal to the length of a lattice cell. The optimum value for the LCLS β-function requires that the lattice cell need to be much shorter than the betatron-oscillation period, therefore, these modulations afflict large transverse angles to the outer beam electrons, resulting in a spread of the phases of the electrons with respect to the ponderomotive potential. For LCLS parameters this de-phasing has an affect on gain and is included in the simulations.

The choice of the FODO cell length is generally driven by a compromise between a reduction in envelope modulation amplitude

$$\Delta\beta_{x,y} / \beta_{x,y} = \frac{1}{2}(\beta_{x,y,\max} - \beta_{x,y,\min}) / \beta_{x,y}, \qquad \textbf{(5.13)}$$

which favors smaller cell lengths and a beam steering argument which favors longer cell lengths. The cell length needs to be smaller than the desired average β-function value. For the LCLS, a cell length of about 7.3 m was chosen (the FODO lattice consists of a number of different cell lengths as discussed below) using the considerations described above for the high-energy (i.e., short wavelength) end of the operational range where it is most important. This cell length is too long for the other low energy (long wavelength) end of the operational range, where is limits the minimum achievable average β-function to the value of the FODO cell spacing, about 7.3 m. As can be seen from **Figure 5.5**, the impact of the increased β-function at lower energies is small.

The integrated quadrupole-strength needed to achieve the average β-function of 18 m at 14.35 GeV is

$$\int_0^{L_{QF}} \frac{dB_{Q_F}}{dr} ds = 5.36\,\mathrm{T} \qquad \textbf{(5.14)}$$

$$\int_0^{L_{QD}} \frac{dB_{Q_D}}{dr} ds = -5.30\,\mathrm{T}\,, \qquad \textbf{(5.15)}$$

for the focusing and the defocusing quadrupoles, respectively. With the quadrupole length of 5 cm, as described in **Chapter 8**, the quadrupole gradients will than be

$$\frac{dB_{Q_F}}{dr} = 107.1\,\mathrm{Tm} \qquad \textbf{(5.16)}$$

$$\frac{dB_{Q_D}}{dr} = -105.9\,\mathrm{Tm}\,, \qquad \textbf{(5.17)}$$

The difference in the two gradients comes from the fact that, as explained above, the undulator segments provide additional, natural focusing but only in the vertical plane. Without the undulator segments the two gradients would be ±109.4 Tm. The gradients, given in **Equations (5.16)** and **(5.17)**, are adequate to achieve the average β-function amplitude of 7.3 m at 4.54 GeV, as well. As explained in **Chapter 8,** permanent magnet quadrupoles will be used. **Figure 5.6** and **Figure 5.7** show the average β-function over the full operational range. The bold line shows the actual values of the average β-function, limited towards lower energies (or longer wavelength) by the FODO cell length. The dotted line shows the values that the quadrupoles could in principal achieve and the dot-dash line shows the values needed for shortest saturation length.

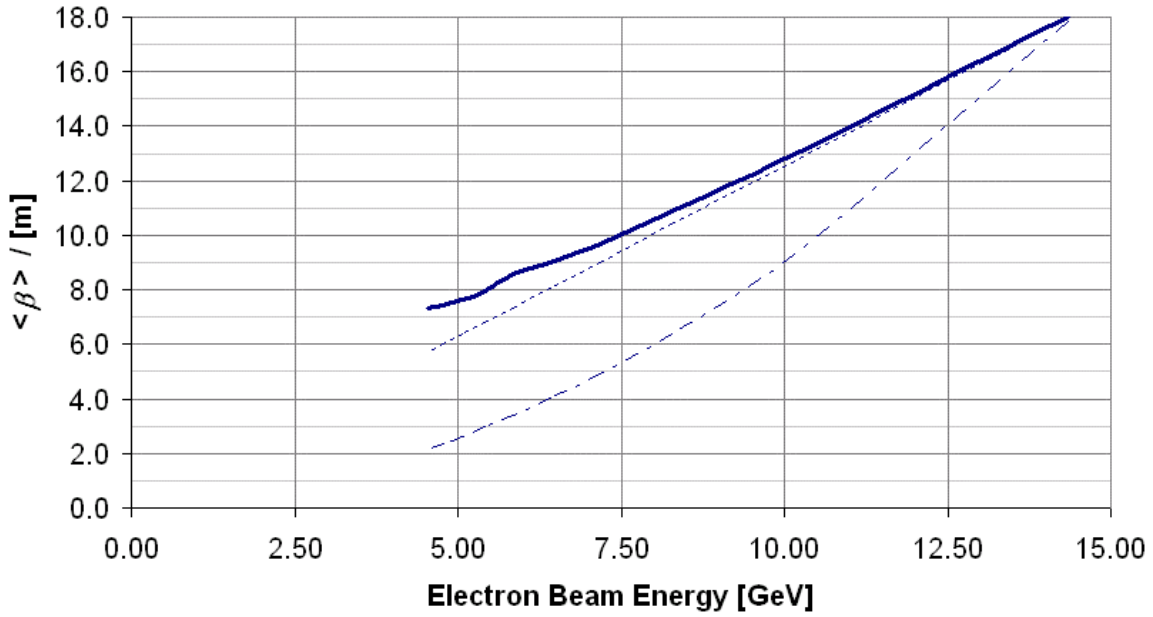

Figure 5.6 Average of the horizontal and vertical β-functions as a function of beam energy using permanent magnet quadrupoles and matching the electron beam focusing into the undulator (solid line). As the β-function amplitude comes close to the length of the FODO cell its dependence on energy deviates from linear (dotted line) by a small amount. The optimum β-function that gives the shortest saturation length (dash-dot line) has a similar dependence but increases faster with energy. The actual β-function stays sufficiently close to the optimum as can be seen from **Figure 5.4** and **Figure 5.5**.

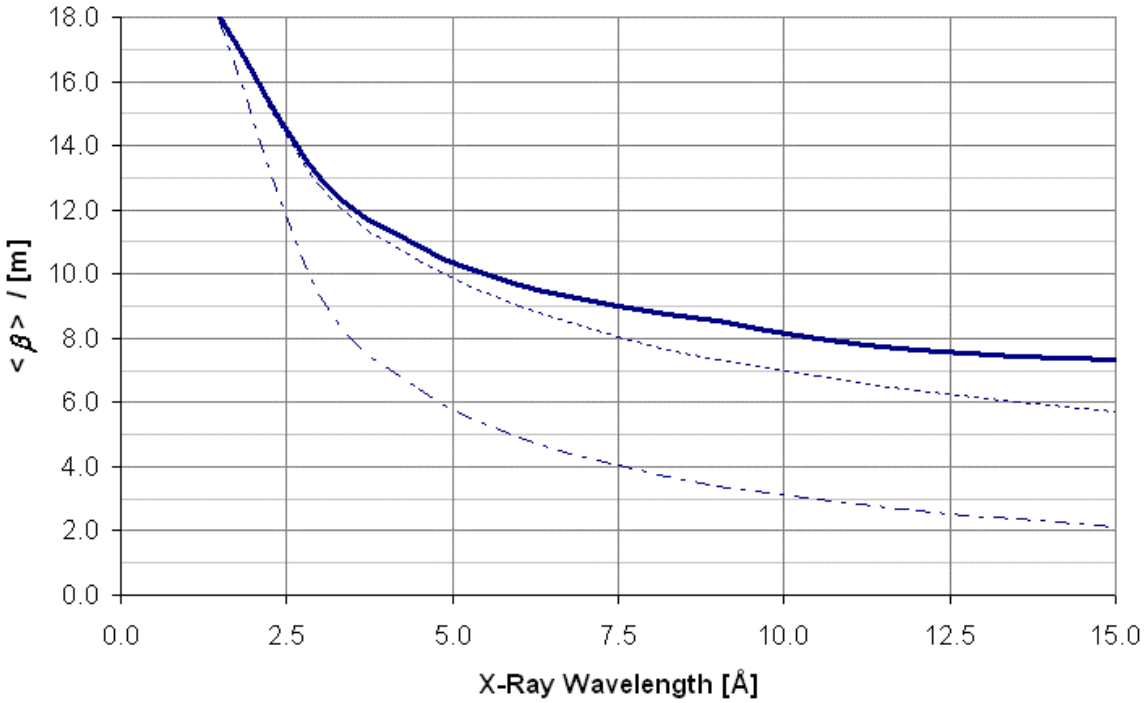

Figure 5.7 Same as **Figure 5.6**, except that the dependence to x-ray wavelength instead of energy is shown.

The horizontal and vertical β-functions, along the entire LCLS undulator, are shown in **Figure 5.8** and **Figure 5.9** for 14.35 GeV and 4.54 GeV, respectively.

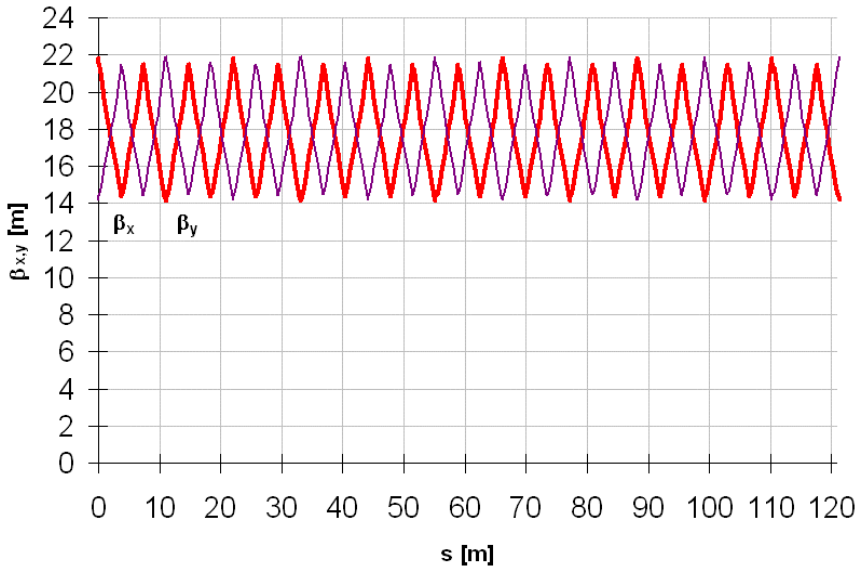

Figure 5.8 Horizontal and vertical β-functions in the LCLS at the high-energy limit of 14.35 GeV.

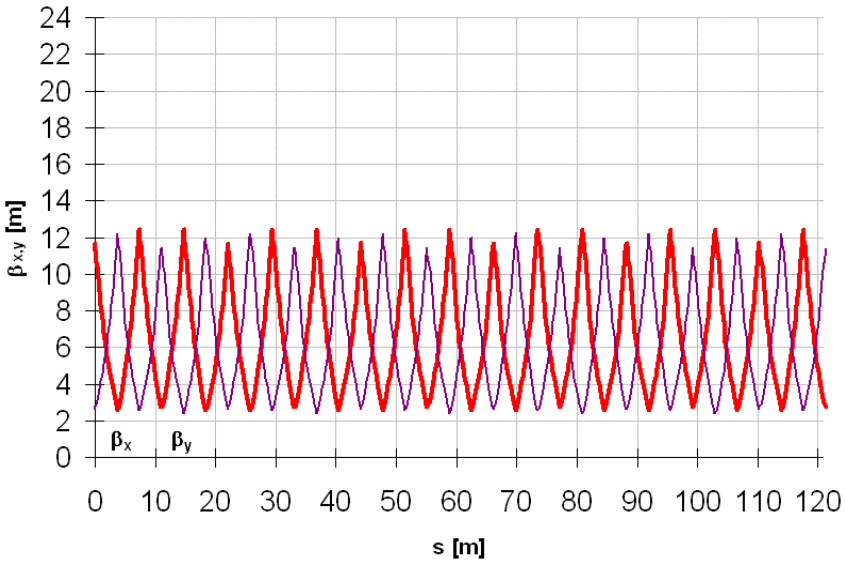

Figure 5.9 Horizontal and vertical β-functions in the LCLS at the low-energy limit of 4.54 GeV.

Both sets of β-functions are generated with the same set of quadrupole strengths; only the matching optics into the undulator has been changed.

5.3.4 FODO Lattice Layout

As described in **Chapter 8**, the LCLS undulator has a total of 33 undulator segments, separated by short breaks. The breaks are used to house the FODO lattice quadrupoles and for other purposes. Not all breaks are of the same length. Five different break lengths are used. Consequently, there is a number of different FODO cell lengths, as well. Except for the beginning of the undulator there is a regular pattern of two short and one long break length. The three break-length period and the two-quadrupole periods (Q_F, Q_D) generate a superperiod of 6 quadruples (and 6 undulator segments) or three FODO cells of lengths 7.311 m, 7.311 m, and 7.428 m. The last 5.5 superperiods are of that structure. The very first three break lengths have been optimized for reduced saturation length and are therefore different from the rest. Consequently the lengths of the three FODO cells of the first "superperiod" are 7.463, 7.5145 m, and 7.311 m. The superperiod structure is reflected in the beating the β-functions in **Figure 5.8** and **Figure 5.9**.

5.4 Computer Simulations

5.4.1 FEL Simulations Codes

Although a three-dimensional theory has been developed and allows the study of the effect of parameters like energy spread, emittance, and diffraction, the effects of magnet errors, misalignment, wakefields and realistic electron distributions can not be treated analytically, yet. For this reason, after one has used 3-D theory to search and optimize the basic parameters of an FEL, the most important tools for a subsequent and more precise study and optimization are the

computer simulation codes [6,7]. Simulations for this design report used the 3-D codes GENESIS 1.3 [8], GINGER [9] (both time dependent), FRED-3D [10] (magnet error analysis, beam position control), as well as the linear code RON [11,12] (magnet tolerances). The codes been extensively cross checked [13] with each other as well as with experimental results from the LEUTL [14] and VISA [15] experiments.

5.4.2 Start-To-End Simulations

The overall system performance has been studied using start-to-end simulations [16]. The beam is transported from the injector through the linac and the undulator using the computer codes, PARMELA (Injector), ELEGANT (Linac) and GENESIS 1.3 (Undulator). The PARMELA code includes space charge, rf, and thermal emittance effects.

Two cases have been considered. One has a charge of 0.25 nC, and a bunch compression set to produce a peak current of about 1.5 kA. In this case the charge has been chosen using the scaling arguments discussed in **Chapter 4**, to provide the optimum beam emittance and brightness. The other case has a charge of 1 nC and a peak current at the LCLS reference case.

5.4.2.1 Case I - Low Charge Limit

In the first case, the normalized emittance is about 0.3 μm-rad. The results, at the linac exit, are shown in **Figure 5.10** and **Figure 5.11**. The first figure gives a "slice" description of the beam, showing various quantities along the longitudinal bunch coordinate.

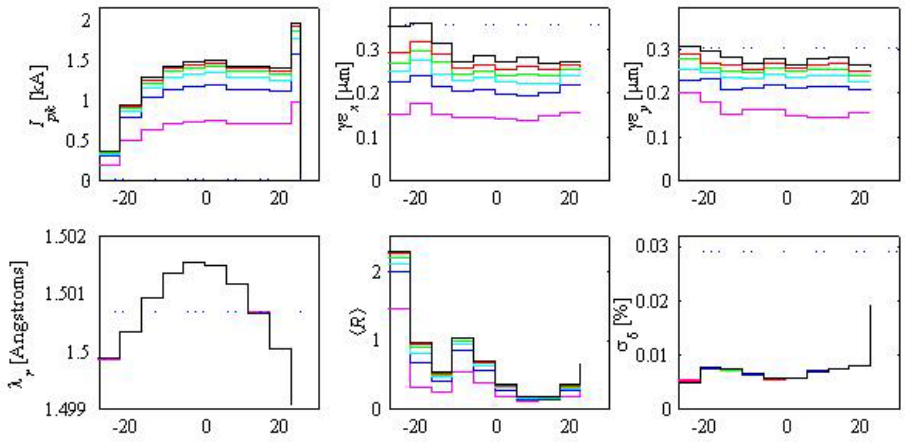

Figure 5.10 Peak current, horizontal and vertical normalized rms slice emittances, equivalent resonant wavelength, Courant-Snyder invariant, and rms slice energy spread along the electron bunch at the undulator entrance. The horizontal axis gives longitudinal position along the bunch in micrometer.

The <*R*> parameter describes the displacements of the transverse centroid of the electron distribution along the bunch. It is defined per slice, using the Courant-Snyder invariant, as:

$$\langle R \rangle = \sqrt{\frac{x^2 + (x\alpha_x + x'\beta_x)^2}{\varepsilon_x \beta_x} + \frac{y^2 + (y\alpha_y + y'\beta_y)^2}{\varepsilon_y \beta_y}} \qquad \textbf{(5.18)}$$

where β_x, β_y, α_x, and α_y are the nominal projected beta and alpha functions per plane, and ε_x, and ε_y are the rms emittances per plane. With the given definition, <*R*> takes on the value of one for a horizontal or vertical displacement of amplitude equal to 1 sigma, as for instance in the case when $x = (\beta_x \varepsilon_x)^{1/2}, x' = 0, y = 0, y' = 0$. Transverse displacements can be due to effects such as coherent synchrotron radiation produced in the linac compressors.

An examination of **Figure 5.10** shows that the emittance is around 0.3 μm-rad, and the corresponding current is about 1.5 kA for most of the bunch. It is also interesting to notice that the electron energy distribution along the bunch produces a wavelength variation of about 0.1%, larger than the expected x-ray SASE linewidth. The graph of <*R*> shows that the compression process produces a transverse displacement of the electrons along the bunch of the order of 1σ. This displacement has an effect on the gain, and also gives a larger x-ray spot size at the undulator exit. This has been accounted for in the brightness estimate.

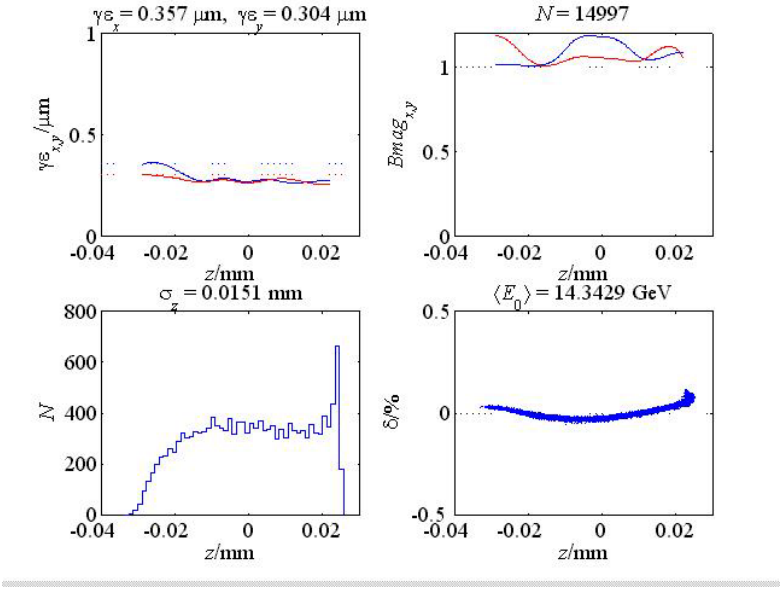

Figure 5.11 Electron beam characteristics at the linac exit for the 0.25-nC case.

Figure 5.11 shows the longitudinal dependence of a set of beam parameters. The quantity B_{mag} describes the local variation of the individual slice phase space ellipses with respect to the projected phase space ellipse. A value of 1 corresponds to a full overlap.

The results of propagating the beam through the undulator is shown in **Figure 5.12** and compared with the case of an "ideal beam" having uniform longitudinal distribution and a Gaussian transverse distribution. As one can see, the real effects, introduced by beam dynamics in the injector-linac-compressor systems, result in a loss of output power. The power in the reference case is 16.6 GW, and in the start-to-end case is 12.1 GW. This calculation does not include undulator wakefields, which have been estimated in **Section 4.5.2**. Note that there is no change in saturation length.

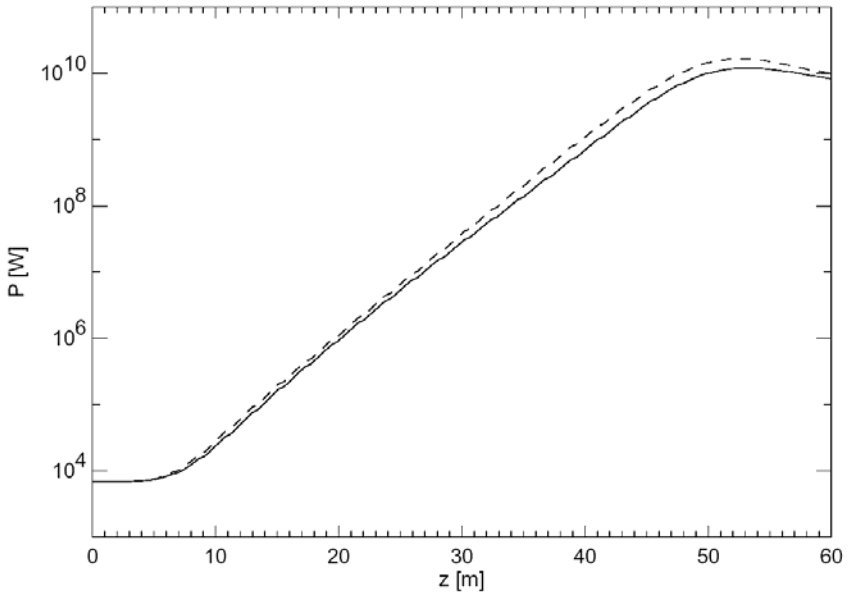

Figure 5.12 Power vs. undulator length for a 0.25-nC case, with an emittance of 0.3 μm-rad and a peak current of 1.5 kA. No undulator wakefields have been included. The dashed line assumes a constant value of emittance and current along the bunch. The effect of using the longitudinal and transverse phase-space distribution produced in the gun-linac-compressor system (solid line) is a reduction in output saturation power.

The distribution of power along the bunch obtained in the start-to-end simulation is shown in **Figure 5.13**. The transverse displacement along the bunch and other effects produce a non-uniform power distribution.

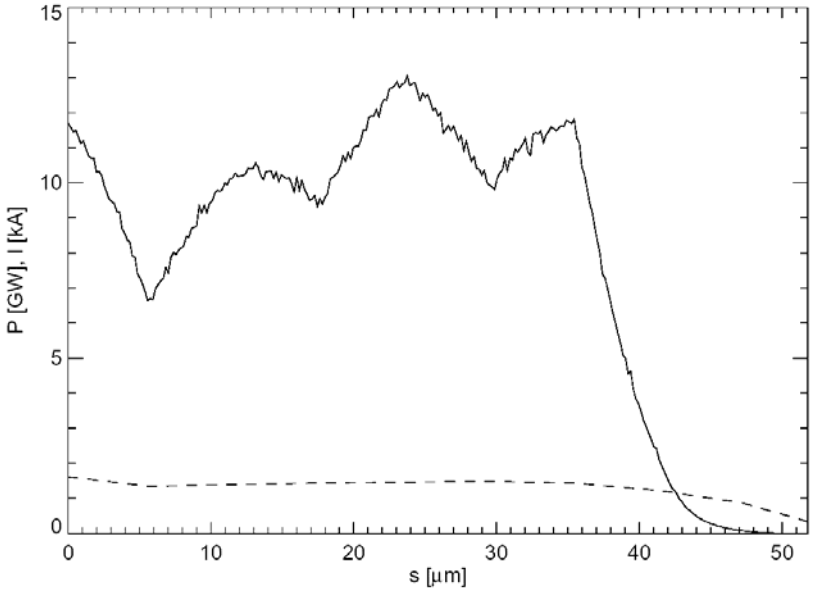

Figure 5.13 Power distribution at saturation (solid) along the electron bunch for the start-to-end simulations for a charge of 0.25 nC. The dashed curve is the current profile in kilo-Amperes. The head of the bunch is to the right.

5.4.2.2 Case II - High Charge Limit

The case of 1 nC is shown in Figure 5.14, Figure 5.15 and Figure 5.16. The first of these figures shows the characteristics of the electron bunch at the undulator entrance, the second the FEL evolution along the undulator, and the third the power distribution along the bunch.

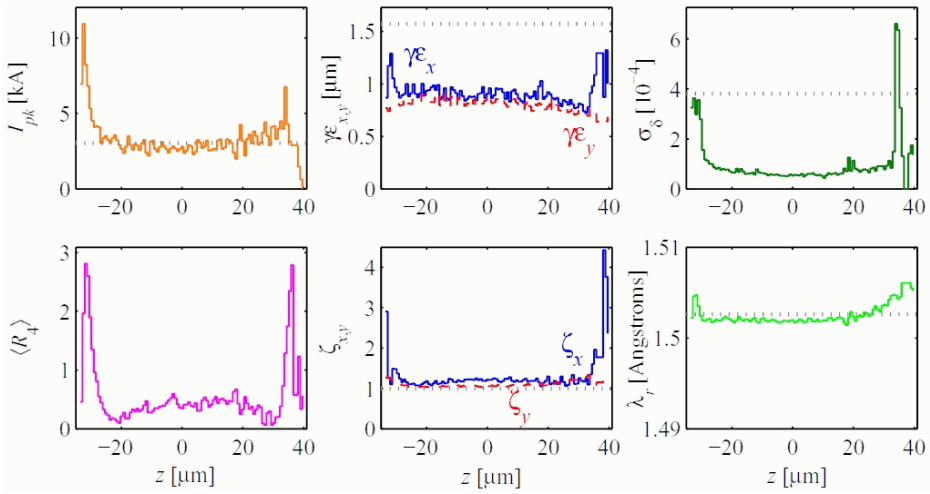

Figure 5.14 Electron beam characteristics at the linac exit for the 1 nC case. The horizontal axis gives longitudinal position along the bunch in μm.

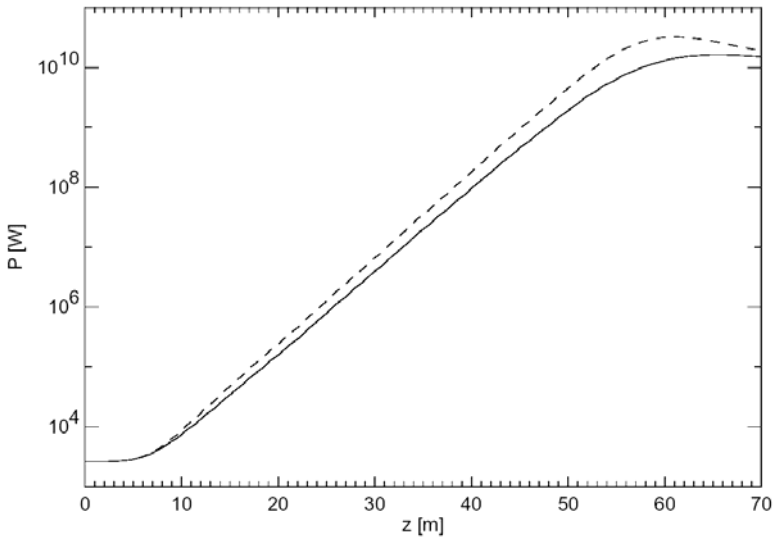

Figure 5.15 The dashed curve is the power vs. undulator length, in meters, for the "ideal" 1-nC case, with an emittance of 0.5-μm rad, and a peak current of 3.4 kA. The solid curve is the start-to-end 1-nC case. The saturation power is 32 GW in the ideal case and 16 GW in the start-to-end case. No undulator wakefields have been included.

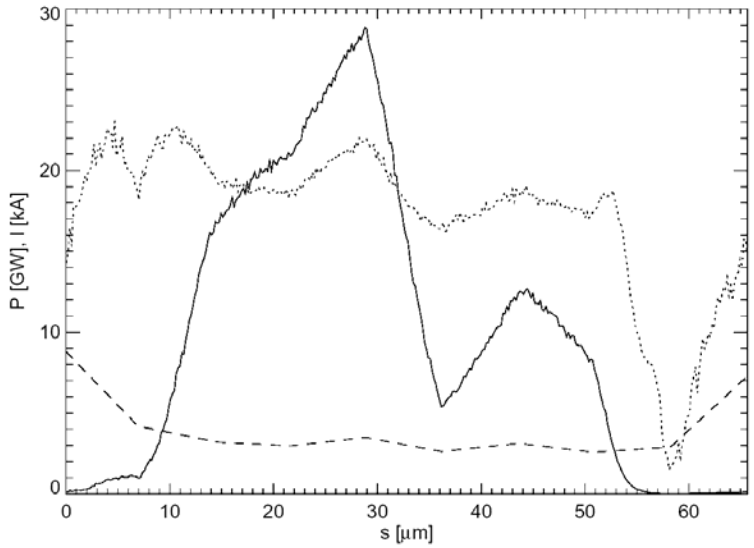

Figure 5.16 Power distribution along the bunch at saturation (solid line), and at a distance 100 m after saturation (dotted line). The dashed line depicts the current profile in units of kA. The head of the bunch is to the right.

5.5 Sources of Gain Reduction

5.5.1 Undulator Trajectory Errors

This section discusses the sensitivity of LCLS FEL performance on imperfections of the electron orbit in the undulator.

5.5.1.1 Undulator Steering and Corrector Description

As shown in detail in **Chapter 8**, the undulator is designed as a planar NdFeB hybrid structure with a period of 3 cm and a full gap height of 6 mm. 113 undulator periods form a 3.375-m long segment (Spacing between the centers of the first and last pole). Segments are separated by breaks that accommodate electron beam position monitors as well as 5-cm long permanent magnet quadrupoles with a gradient of about 107 T/m. The quadrupoles are used for two purposes, electron beam focusing and steering. Steering is achieved by adjusting the quadrupoles' x and y positions with stepper-motor based systems that allow a total movement of 0.5 mm with a step size of 1 μm. The undulator is built from 33 segments resulting in a total length of about 121 m, of which about 112.86 m is magnet length.

5.5.1.2 Magnetic Field Errors

The sources of magnetic field errors in the LCLS undulator are from misaligned quadrupoles, undulator pole errors, the earth field, and other stray fields. The misalignment of the quadrupoles has been strongly reduced by design. As described above, their transverse position can be remotely adjusted and is used for beam steering. The finite resolution of the movers is compensated by auxillary horizontal and vertical steering magnets. The effect of the earth field is small and will be corrected by beam-based-alignment. Stray fields will be avoided or minimized

by design. The potentially most significant sources of FEL performance reduction come from errors in the on-axis magnetic field of the undulator and from dipole components of transversely misaligned quadrupoles. As shown in **Chapter 8** these magnet errors can be strongly reduced by state-of-the-art sorting and shimming techniques.

5.5.1.3 Undulator Trajectory Straightness Tolerances

Radiation produced from the electron distribution emerges collinear to the electron beam path. In an ideal undulator, the electron beam executes transverse wiggle oscillations in the periodic magnetic field of the undulator along a straight line, causing the electron beam and the radiation pulse to travel on average on the same path with optimum transverse overlap. The electrons' wiggle motion reduce their z-velocity just enough to move exactly one optical wavelength for each undulator period traveled, effectively keeping the two components in phase. Both aspects are necessary for optimum gain. Field errors can cause the electron beam to deviate from the ideal trajectory, which reduces the overlap between the electron distribution and the radiation. It also moves the phases of the electrons with respect to the ponderomotive potential well. Based on computer simulations a transverse displacement by about 1 rms beam radius or a phase slip of 18 degrees of optical wavelength per power gain length both cause the saturation length to increase by one power gain length. While the beam radius does not depend very strongly on the radiation wavelength, the phase slip for a given trajectory is inversely proportional to the wavelength. Thus, while, at long wavelengths, the overlap aspect often dominates the tolerance, in contrast, at x-ray wavelengths, the phase slip dominates the tolerance. The 18 degrees per power gain length is reached for the LCLS at 1.5 Å with an rms trajectory amplitude of about 2 μm. Although this absolute accuracy seems difficult to achieve, it will be shown in **Section 8.12** that it is obtainable with a beam-based alignment technique.

5.5.1.4 Steering Stations Separations

After the application of the beam-based alignment procedure the transverse position of the electron BPMs will be calibrated using the straight beam. Between two applications of the procedure the beam trajectory will be corrected by adjusting the transverse position of the quadrupoles based on the readings of the calibrated electron BPMs, setting tolerances for the resolution of the BPMs and the relative spacing of the steering stations, i.e., the combination of steerer quadrupole and BPM. Limited BPM resolution will force the beam on a zigzag trajectory between steering stations. If the steering stations are spaced too closely the effect gets amplified. On the other hand, if the steering stations are spaced too far apart, the undulator pole errors are not sufficiently corrected. There is an optimum for the separation of steering stations [17], which depends on the BPM resolution and the pole error. The smaller the pole errors the shallower is the optimum. As described in **Chapter 8**, the steering station separation for the LCLS has been chosen around the optimum.

5.5.1.5 Undulator Trajectory Matching Tolerances

The match of the electron trajectory at the entrance and end of each undulator section is done by making the strength of the end poles in the sequence ¼, ¾, 1, and -1 times the strength the

regular pole (see **Chapter 8**, **Section 8.5.3)**. The "matching sections," which are off resonance, do not contribute to lasing but will add a small phase shift, which reduces the space of the actual separation by a few centimeters. Estimates based on beam size arguments indicate that position and angle errors of about 5 μm and 1 μrad, respectively, should not affect FEL performance. These tolerances can be achieved with state-of-the-art instrumentation (see **Chapter 7**).

5.5.2 Effects of the Emission of Spontaneous Radiation on Gain

Due to the rather large value of the undulator parameter, *K*, synchrotron radiation from the electron beam in the FEL undulator not only occurs at the resonant frequency and its harmonics but over a wide continuous spectrum of frequencies. As long as micro bunching can be neglected, the total peak synchrotron power radiated by a bunch is given by [18]

$$\hat{P}_{spont} = Z_o I_{pk} e \frac{2\pi c}{6\lambda_u} \gamma^2 K^2 N_u = 0.663 \cdot 10^{-15} \cdot \frac{s}{(Tm)^3} \cdot (E/e)^2 B_u^2 L_u I_{pk} \qquad \textbf{(5.19)}$$

The power from spontaneous radiation grows linearly along the undulator up to $\hat{P}_{spont} = 96$ GW after 120 m at 1.5 Å. This is more than ten times as much as can be expected for the fundamental peak of the coherent FEL radiation. While this large amount of incoherent radiation by itself makes the LCLS the brightest x-ray source available, it is undesirable when the LCLS is to be tuned for FEL lasing. Not only can it cause problems for the x-ray optics, but it also reduces the average electron energy, increases the incoherent energy spread and the emittance, and adds extra heat load to components that might be installed along the undulator for diagnostics and beam filtering purposes.

5.5.2.1 Average Energy Loss

The average energy loss $\Delta\langle\gamma\rangle$ from spontaneous synchrotron radiation for each electron is

$$\Delta\langle\gamma\rangle = -\frac{\hat{P}_{spont}}{I_{pk}} \frac{e}{mc^2} = -\frac{1}{3}\gamma^2 K^2 k_u^2 L_u \qquad \textbf{(5.20)}$$

where $k_u = 2\pi/\lambda_u$, which causes the electrons to move away from the resonance. The resonant frequency of the radiation can be kept constant by reducing the magnetic field along the undulator (micro-tapering). The amount of field taper required is

$$\Delta B_u / B_u = \frac{1 + K^2/2}{K^2/2} \Delta\langle\gamma\rangle / \langle\gamma\rangle \qquad \textbf{(5.21)}$$

Table 5.3 Reduction in average energy and required amplitude of micro-tapering, $\Delta B_u/B_u$, due to random photo-emission process in spontaneous undulator radiation in the LCLS for the two limits of the operational wavelength range.

λ_r	I_{pk}	$\Delta\langle\gamma\rangle$	$\langle\gamma\rangle$	$\Delta\langle\gamma\rangle/\langle\gamma\rangle$	$\Delta B_u/B_u$
1.5 Å	3400 A	-46	28077	-1.64×10^{-3}	-1.9×10^{-3}
15 Å	3400 A	-1.38	8879	-1.56×10^{-4}	-1.8×10^{-4}

The loss in average beam energy, $\Delta\langle\gamma\rangle/\langle\gamma\rangle$, at the 1.5-Å (14.35 GeV) end of the operational range is large enough to move the particles outside the FEL gain-bandwidth. Micro-tapering of the undulator segments will be required. The actual required change in magnetic field is very small. It is not necessary to taper the individual undulator segments, but the average field of each segment needs to be a bit smaller than the preceding segments. The required field taper at the high energy end of the operational range will be a bit too large for the low energy end of the range, where it will cause a small reduction in gain unless the taper is adjustable.

5.5.2.2 Energy Spread Increase

The statistical nature of the synchrotron radiation process increases the incoherent energy spread of the electrons by [19]:

$$d<\Delta\gamma^2>=\frac{14}{15}\frac{\lambda_c}{2\pi}r_e\gamma^4k_u^3K^2F(K)L_u \qquad \textbf{(5.22)}$$

where $F(K)\approx 0.6K$ for $K>>1$ and for a planar undulator. λ_c is the Compton wavelength ($\lambda_c/2\pi\approx 3.862\times10^{-13}$). The amplitudes of the effect are shown in **Table 5.4**. The largest influence on FEL performance for the LCLS occurs at the high-energy end.

Table 5.4 Influence of Compton wavelength on FEL performance.

γ	L_w	$\sqrt{d<\Delta\gamma^2>}$
28082	100 m	6.5
8880	80 m	0.36

There, the energy spread increase due to incoherent synchrotron radiation will reach the level of the initial rms energy spread which is σ_γ= 2.88. Simulations with the code GENESIS 1.3 show no reduction in performance.

5.5.2.3 Emittance Increase

Spontaneous synchrotron radiation can cause an increase in rms beam emittance if the radiation occurs at a location with a finite dispersion function [20]. The dispersion function originates in the undulator, is of the order of the wiggle amplitude (~1 μm), and has a negligible effect on the emittance.

5.6 Electron Beam Tolerances

5.6.1 Electron Beam Tolerance Goals

This CDR uses a number of goal parameters for emittance and energy spread both as electron bunch slice quantities and projected quantities as defined in **Section 5.2.2**. These numbers are larger than those predicted by computer simulations. Establishing parameter goals decouples the design processes of the various FEL subsystems. The numbers are listed in **Table 5.5** at two points in the FEL line, after the Injector and at the entrance to the undulator. The exception is the Projected Energy Spread, which is not relevant before the entrance to the undulator.

Table 5.5 Goals for basic LCLS Beam Parameters for a beam charge of 1 nC. The numbers at the Undulator Entrance are for a beam energy of 14.35 GeV.

Parameter	Location	LCLS Goal Value
Slice Emittance	Injector (@150 MeV)	1.0 mm mrad (RMS)
	Undulator Entrance	1.2 mm mrad (RMS)
Projected Emittance	Injector (@150 MeV)	1.2 mm mrad (RMS)
	Undulator Entrance	1.5 mm mrad (RMS)
Slice Energy Spread	Injector (@150 MeV)	0.01 % (RMS)
	Undulator Entrance	0.01 % (RMS)
Projected Energy Spread	Undulator Entrance	0.06 % (RMS)

In particular for the Slice Energy Spread, the goals have been limited to a level that is believed to be measurable even though simulations indicate that smaller levels could be achieved. A summary of Measurement Accuracy Goals and Precision Goals is given in **Table 5.6** and

Table 5.7.

Table 5.6 Electron Beam Measurement Accuracy Goals for Absolute LCLS Parameters.

Parameter	Location	Parameter Range	Relative Accuracy
Bunch Charge	Inj., DL2 and Dump	0.1-1.0 nC	1 %
Bunch Length	After BC2 (~5 GeV)	20-40 μm	10 %
Projected Rel. Energy Spread	DL2 (14.35 GeV)	0.02-0.1 %	20 %
'Slice' Rel. Energy Spread	DL2 (14.35 GeV)	0.01 % or larger	30 %
Projected Emittance	Inj., BC1, BC2, DL2	0.3-3 mm mrad	20 %
'Slice' Emittance	After BC2	0.2-2 mm mrad	30 %
Electron Beam Energy	DL2 or Dump	4.5-15 GeV	2 %

Table 5.7 Shot-to-Shot Precision Goals for LCLS Beam Parameters.

Parameter	Location	Parameter Range	Relative Precision
Bunch Charge	Inj., DL2 and Dump	0.1-1.0 nC	~0.1 %
Bunch Length	After BC2 (~5 GeV)	20-40 μm	~5 %
Projected Rel. Energy Spread	DL2 (14.35 GeV)	0.02-0.1 %	~5 %
'Slice' Rel. Energy Spread	DL2 (14.35 GeV)	0.01 % or larger	~10 %
Projected Emittance	Inj., BC1, BC2, DL2	0.3-3 mm mrad	~10 %
'Slice' Emittance	After BC2	0.2-2 mm mrad	~15 %
Electron Beam Energy	DL2 or Dump	4.5-15 GeV	7×10^{-3} %

Parameter	Location	Parameter Range	Relative Precision
Pulse Arrival Time	Undulator	-	50 fs

5.6.2 Pulse-To-Pulse Intensity

In addition to the intensity fluctuations produced by the statistical nature of the SASE process, about 6% for the LCLS case as described in **Chapter 4**, there will be intensity jitter in the x-ray radiation due to intensity jitter of electron beam parameters, i.e. random changes from shot to shot of electron beam charge, current, emittance, energy spread. Charge fluctuations induce correlated changes in the other beam parameters, like emittance and current. However, fluctuations in bunch length and energy spread, not correlated to the charge, are also induced by jitter in the laser pulse arrival time with respect to the linac-rf, and by changes in the longitudinal and transverse charge distribution. These can be produced by changes in the laser pulse profile at the photo-cathode, and by changes in the laser centroid, or by the photoemission process. The effect of changes in the beam parameters affects the radiation intensity in one way if the FEL reaches saturation, and in a stronger way if saturation is not reached.

5.6.2.1 Jitter at Saturation

Table 5.8 and **Table 5.9** show the sensitivities of the saturation power and saturation length to various FEL parameters at 1.5 Å (14.35 GeV). They are given in the forms

$$\frac{\Delta P_{sat} / P_{sat}}{\Delta \varepsilon_n / \varepsilon_n} = -1.5 \tag{5.23}$$

and

$$\frac{\Delta L_{sat} / L_{sat}}{\Delta \varepsilon_n / \varepsilon_n} = 0.8, \tag{5.24}$$

which means that increasing the normalized emittance by 10 %, i.e., $\Delta \varepsilon_n / \varepsilon_n = 0.1$, will reduce the saturation power by 15 %, i.e., $\Delta P_{sat} / P_{sat} = -0.15$.

The last three table rows are of relevance for jitter considerations. Notice the strong sensitivities of the saturation length to peak current and normalized emittance. The first four table rows are relevant for FEL design considerations. One can see that system fluctuations can be easily larger than SASE fluctuations.

Measuring the gain length, whose value depends on the system fluctuations but not on the SASE fluctuations, will give direct information on the effect of system fluctuations on the FEL. Using this information and making statistically significant intensity measurements for well-defined set of beam parameters, one will be able to separate the system and SASE fluctuations and monitor the intensity at each shot.

Table 5.8 LCLS sensitivities to input parameters at 1.5 Å.

$\frac{\Delta P_{sat} / P_{sat}}{\Delta\lambda_\gamma / \lambda_\gamma} = 0.56$ (variable γ_r)	$\frac{\Delta L_{sat} / L_{sat}}{\Delta\lambda_\gamma / \lambda_\gamma} = -0.6$ (variable γ_r)
$\frac{\Delta P_{sat} / P_{sat}}{\Delta\lambda_u / \lambda_u} = 3.6$ (variable γ_r)	$\frac{\Delta L_{sat} / L_{sat}}{\Delta\lambda_u / \lambda_u} = 0.3$ (variable γ_r)
$\frac{\Delta P_{sat} / P_{sat}}{\Delta\beta_{x,y} / \beta_{x,y}} = 0.4$	$\frac{\Delta L_{sat} / L_{sat}}{\Delta\beta_{x,y} / \beta_{x,y}} = 0.0$
$\frac{\Delta P_{sat} / P_{sat}}{\Delta\gamma / \gamma} = 1.9$ (variable gap)	$\frac{\Delta L_{sat} / L_{sat}}{\Delta\gamma / \gamma} = -0.3$ (variable gap)
$\frac{\Delta P_{sat} / P_{sat}}{\Delta\sigma_\gamma / \sigma_\gamma} = -0.1$	$\frac{\Delta L_{sat} / L_{sat}}{\Delta\sigma_\gamma / \sigma_\gamma} = 0.0$
$\frac{\Delta P_{sat} / P_{sat}}{\Delta\varepsilon_n / \varepsilon_n} = -1.5$	$\frac{\Delta L_{sat} / L_{sat}}{\Delta\varepsilon_n / \varepsilon_n} = 0.8$
$\frac{\Delta P_{sat} / P_{sat}}{\Delta I_{pl} / I_{pk}} = 1.8$	$\frac{\Delta L_{sat} / L_{sat}}{\Delta I_{pl} / I_{pk}} = -0.5$

Table 5.9 LCLS sensitivities to input parameters at 15 Å.

$\frac{\Delta P_{sat} / P_{sat}}{\Delta\lambda_\gamma / \lambda_\gamma} = 0.0$ (variable γ_r)	$\frac{\Delta L_{sat} / L_{sat}}{\Delta\lambda_\gamma / \lambda_\gamma} = -0.4$ (variable γ_r)
$\frac{\Delta P_{sat} / P_{sat}}{\Delta\lambda_u / \lambda_u} = 2.8$ (variable γ_r)	$\frac{\Delta L_{sat} / L_{sat}}{\Delta\lambda_u / \lambda_u} = 0.6$ (variable γ_r)
$\frac{\Delta P_{sat} / P_{sat}}{\Delta\beta_{x,y} / \beta_{x,y}} = -0.2$	$\frac{\Delta L_{sat} / L_{sat}}{\Delta\beta_{x,y} / \beta_{x,y}} = -0.2$
$\frac{\Delta P_{sat} / P_{sat}}{\Delta\gamma / \gamma} = 1.2$ (variable gap)	$\frac{\Delta L_{sat} / L_{sat}}{\Delta\gamma / \gamma} = 0.0$ (variable gap)
$\frac{\Delta P_{sat} / P_{sat}}{\Delta\sigma_\gamma / \sigma_\gamma} = -0.2$	$\frac{\Delta L_{sat} / L_{sat}}{\Delta\sigma_\gamma / \sigma_\gamma} = 0.0$
$\frac{\Delta P_{sat} / P_{sat}}{\Delta\varepsilon_n / \varepsilon_n} = -1.5$	$\frac{\Delta L_{sat} / L_{sat}}{\Delta\varepsilon_n / \varepsilon_n} = 0.8$

$\frac{\Delta P_{sat} / P_{sat}}{\Delta I_{pl} / I_{pk}} = 1.8$	$\frac{\Delta L_{sat} / L_{sat}}{\Delta I_{pl} / I_{pk}} = -0.5$

5.6.2.2 Jitter in the Exponential Gain Regime

The undulator has been designed to be not significantly longer than the expected saturation length at the goal parameters. At the highest energy electron beam energy (corresponding to the shortest radiation wavelength) a deviation from the goal parameters, especially a reduction in peak current and an increase in electron beam emittance, will move the saturation point beyond the end of the undulator. The FEL output will then be determined by the exponential gain regime, resulting in much higher pulse-to-pulse variations.

According to 1-D FEL theory, the derivative of the peak power with respect to the peak current in the exponential gain regime.

$$\frac{dP_{sat}}{dI_{pk}} = \left(1 + \frac{z}{3L_G}\right)\frac{P_{sat}}{I_{pk}} \tag{5.25}$$

The sensitivities as defined in the previous section can be calculated to

$$\frac{\Delta P_z / P_z}{\Delta I_{pk} / I_{pk}} = 1 + \frac{1}{3}\frac{z}{L_G}, \tag{5.26}$$

which can be a large increase compared to the saturation point, which gives

$$\frac{\Delta P_{sat} / P_{sat}}{\Delta I_{pk} / I_{pk}} = \frac{4}{3} \tag{5.27}$$

when making the equivalent calculations. In general, in the exponential gain regime, the sensitivity to fluctuations in peak current increases, as do the sensitivities to fluctuations in normalized emittance and energy spread. The relative sensitivities as obtained from GINGER simulations at 1.5 Å are shown in **Table 5.10**.

Table 5.10 Sensitivities of LCLS performance to electron beam parameters at the end of the 121 m long undulator in the exponential gain regime (at $z/L_G \approx 11.3$ for $I_{pk} = 1500$ A) and at saturation ($I_{pk} = = 3400$ A).

Sensitivity at I=3400 A	**Sensitivity at I=1500 A**
Saturation	**Exponential Gain Regime**
$\frac{\Delta P / P}{\Delta I_{pk} / I_{pk}} = 1.8$	$\frac{\Delta P / P}{\Delta I_{pk} / I_{pk}} = 6.4$
$\frac{\Delta P / P}{\Delta \varepsilon_n / \varepsilon_n} = -1.5$	$\frac{\Delta P / P}{\Delta \varepsilon_n / \varepsilon_n} = -9.3$

$\frac{\Delta P / P}{\Delta\sigma_\gamma / \sigma_\gamma} = 0.2$	$\frac{\Delta P / P}{\Delta\sigma_\gamma / \sigma_\gamma} = -1.8$

The numbers in **Table 5.10** that are based on simulations are larger than those predicted by the 1-D formula, i.e., 1.3 compared to 1.8 at saturation and 4.8 compared to 6.4 at $z/L_G \approx 11.3$ for the sensitivity of peak electron beam current on peak x-ray radiation power. With the expected pulse-to-pulse jitter of the electron beam that as provided by the linac, i.e., $\Delta I_{pk} / I_{pk} \approx$ 10-20%, $\Delta\varepsilon_n/\varepsilon_n \approx 5\%$, $\Delta\sigma_\gamma/\sigma_\gamma < 10^{-5}$, the x-ray power jitter will be large when operating at saturation but will be unacceptable when operating in the exponential gain regime. The peak current therefore may not be a suitable variable for controlling FEL output power. The implications of **Table 5.10** are that the output power at saturation is expected to fluctuate by 20-36%, due mostly to fluctuations in peak current. This fluctuation adds (quadratically) to the natural fluctuations of the SASE process (about 6%; see **Chapter 4**).

5.6.3 Control of X-Ray Power Levels

For applications that use the x-rays, produced by the FEL, it is important that the output power levels be controllable (see **Chapter 9**). The feasibility of changing the output power by varying the peak current was studied.

By changing peak current, either by reducing the amount of charge per pulse or by increasing the pulse length, one can control (reduce) the FEL production over many orders of magnitude. Unfortunately, as the explained in the previous section this action not only reduces the saturation power, but it also increases the saturation length, which undesirably increases pulse-to-pulse jitter.

The conclusion is that the method is not promising. For this reason, a gas absorption cell after the FEL undulator will be used for this purpose. The device is described in detail in **Chapter 9**.

5.7 The Temporal Structure of the X-Ray Pulse

Figure 5.17 shows the simulation results obtained with the time-dependent computer code GINGER. Self-Amplified Spontaneous Emission [21,22] relies on longitudinal electron density fluctuations (shot-noise bunching). Regions where the initial bunching is larger produce more radiation, thus accelerating the lasing process. Due to slippage during the transport through the undulator, those regions will expand to build spikes on the scale of $2\pi L_c = 4\pi L_G \lambda_r / \lambda_u$ [23] as described in **Chapter 4**. The time-dependent simulations clearly show this phenomenon. For the LCLS, the spike structure length is of the order of 0.3 μm at 1.5 Å wavelength and 5 μm at 15 Å.

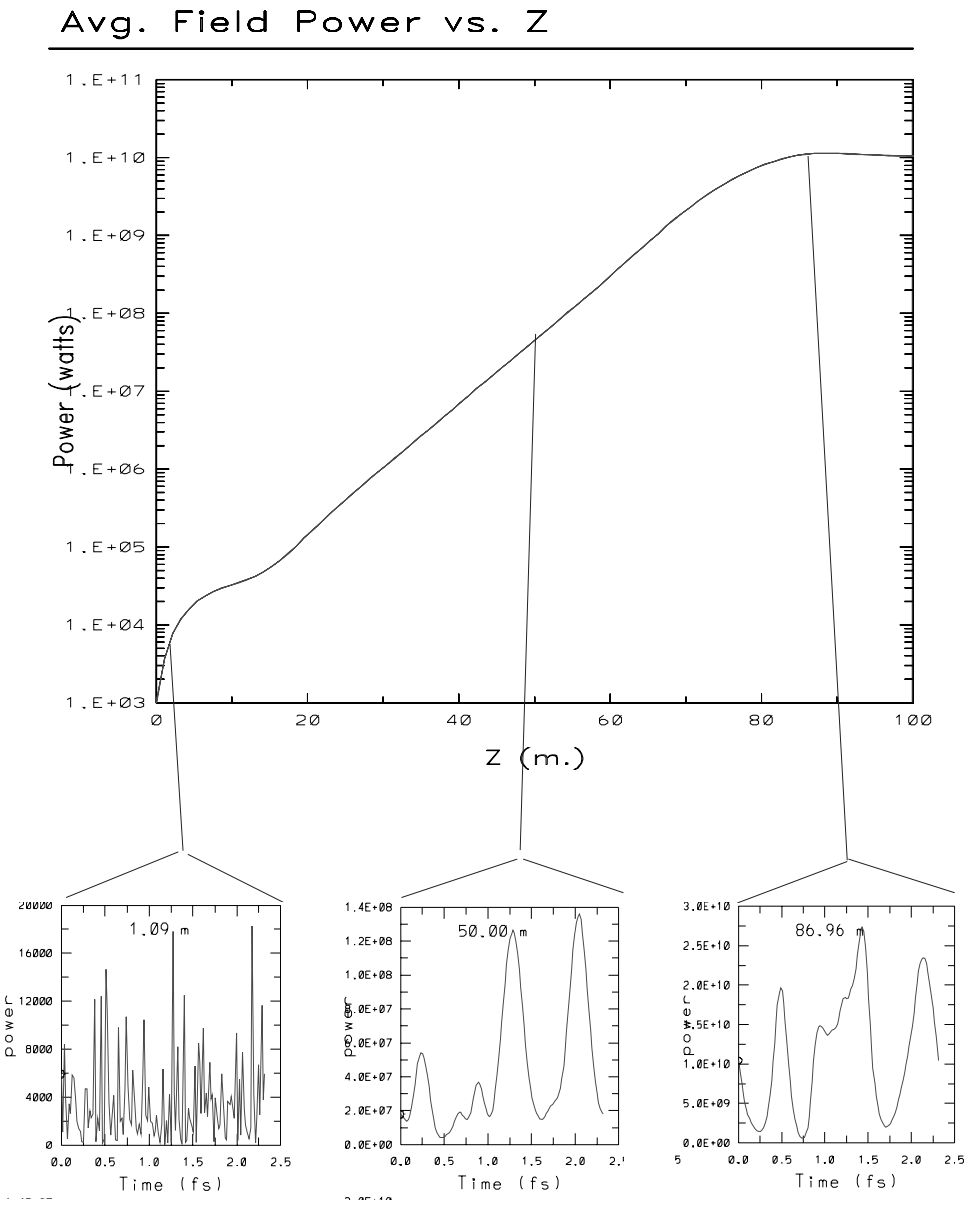

Figure 5.17 FEL output power pattern along the bunch for different position along the gain process.

5.8 LCLS FEL Commissioning

5.8.1 Procedural Aspects of the FEL Gain Commissioning

The commissioning phase of the LCLS will include the following steps:

a. Measurement of the electron beam properties at the undulator entrance as a function of charge and compression.

b. Propagation of the electron beam through the undulator, alignment of the beam and measurement of its transverse distribution at a sufficient number of stations.

c. Measurement of the x-ray radiation intensity, line width, and angular distribution as a function of electron beam parameters to determine FEL gain, intensity fluctuations, spectral and coherence properties and compare them to the theoretical expectations. These measurements can be done at the undulator exit and at several stations along the undulator.

During commissioning and operation, it will be important to monitor the electron beam and x-ray characteristics at each pulse. This is necessary in order to separate the FEL intensity fluctuations due to the SASE start-up from noise — of the order of about 6% for the reference LCLS case — from those due to system fluctuations in the drive laser- electron source-linac system, which can be much larger.

After commissioning is complete, during the LCLS operation, there will still be a need to monitor the electron beam and x-ray characteristic on a pulse-by-pulse basis to provide reference information to the user experiments for data reduction. If this reference information is based on electron beam parameters, the precision will be limited to that of the FEL intensity fluctuation. Monitoring pulse-by-pulse x-ray intensity directly will provide reference information with a higher level of precision.

The electron beam and radiation quantities to be measured for the commission of the LCLS and for a comparison of the FEL properties with theory are:

a. Electron bunch charge

b. Electron bunch center of mass position along the undulator

c. Electron bunch transverse distribution throughout the undulator (as a function of charge)

d. Electron bunch longitudinal distribution as well as integrated and slice energy spread (as a function of charge)

e. X-ray intensity within a defined solid angle and line width as function of electron bunch charge (These measurements can be done at the undulator exit and at several stations along the undulator.)

5.9 Summary

The operating parameters have been optimized by an analysis a three-dimensional algorithm and by computer simulations. The results of the study are that the FEL design objectives are reachable with a 121-m long undulator, and with the beam characteristics given in **Chapter 2, Table 2.4-1**, and in **Appendix A** (parameter list). A study of the effect of the electron beam optics on the FEL performance led to the choice of the FODO lattice cell length and the quadrupole strength. The sensitivity of the FEL performance to the main undulator and electron beam parameters was studied, and from this, tolerances for the pole-to-pole magnetic field variations and for the electron beam characteristics were derived.

5.10 References

1 M. Xie, "Design Optimization for an X-ray Free Electron Laser Driven by SLAC Linac," LBL Preprint No-36038, 1995, also, *IEEE Proceedings for Pac95*, No. 95CH3584, **183**, 1996.

2 K.-J. Kim, "Three-dimensional analysis of coherent amplification and self-amplified spontaneous emission in free electron lasers," *Phys. Rev. Lett.*, **57**, p.1871, 1986.

3 Y.H. Chin, K.-J. Kim, M. Xie, "Three-Dimensional Free Electron Laser Theory Including Betatron Oscillations," LBL-32329, May 1992 49pp and *Phys. Rev*, **A46**, 6662 (1992).

4 L.H. Yu, S. Krinsky, R.L. Gluckstern, "Calculation of Universal Function for Free-Electron Laser Gain," *Phys. Rev. Lett.* **64**, 3011 (1990).

5 L.H. Yu, S. Krinsky, R.L. Gluckstern, J.B.J. van Zeijts, "Effect of wiggler errors on free-electron-laser gain." Phys. Rev. **A45**, 1163, 1992

6 H.-D. Nuhn , "Overview of SASE Free-Electron Laser Simulations Codes." in *Proc. International Society for Optical Engineering, Free Electron Laser Challenges II*, San Jose, CA, Jan 23-27, 1999, (SPIE v. 3614) pp. 119-130.

7 Proceedings of the X-Ray FEL Theory and Simulation Codes Workshop. H.-D. Nuhn and C. Pellegrini (edts.), SLAC, September 23-24, 1999.LCLS-TN-00-1. SLAC-WP-17. (2000).

8 S. Reiche, *Nucl. Instr.. Meth.* **A429**, 243 (1999).

9 W.M. Fawley, Report LBNL-49625 (2002).

10 E.T. Scharlemann, "Wiggle plane focusing in linear undulators," *J. Appl. Phys*., **58**(6), pp. 2154-2161, 1985.

11 R.J. Dejus, O.A. Shevchenko, and N.A. Vinokurov, *Nucl. Instr.. Meth.* **A 429** (1999) 225.

12 R.J. Dejus, O.A. Shevchenko, and N.A. Vinokurov, *Nucl. Instr.. Meth.* **A 445** (2000) 19.

13 S.G. Biedron, Y.C. Chae, R.J. Dejus, B. Faatz, H.P. Freund, S.V. Milton, H.-D. Nuhn, and S. Reiche, "The APS SASE FEL: Modeling and Code Comparison," in Proceedings of the 1999 Particle Accelerator Conference (PAC99), New York City, NY, USA, 1999. *Nucl. Instrum. Meth.* **A 445**, pp. 110-115 (2000).

14 S. V. Milton et al., "Observation of Self-Amplified Spontaneous Emission and Exponential Growth at 530nm", *Phys. Rev. Lett*., **85**, 988-991 (2000), and *Proc. Intern.FEL-2000 Conf*., Duke University (2000).

15 A. Tremaine et al., "Initial Gain Measurements of a 800 nm SASE-FEL, VISA", in *Proc. Intern.FEL-2000 Conf.*, Duke University (2000);

16 M.D. Borland, Y.-C. Chae, J.W. Lewellen, S.V. Milton, R.Soliday, V. Bhradwaj, P. Emma, P. Krejcik, H.-D. Nuhn, W.M. Fawley, "Start-to-End Simulation of SASE FELs from the Gun through the Undulator," in *Proceedings of the 23th International Free Electron Laser Conference and 8th Annual FEL User Workshop*, Darmstadt, Germany, 20-24 Aug 2001.

17 P. Emma, "Electron Phase Slip in an Undulator with Dipole Field and BPM Errors," LCLS-TN-00-14, (October 3, 2000).

18 K.-J. Kim, "Characterization of Synchrotron Radiation," in *X-RAY DATA BOOKLET*, K. Kirz et. al, ed., April 1986, LBNL PUB-490 Rev.

19 S. Reiche, in *Proceedings of the 1997 Workshop,* "Towards X-Ray Free Electron Lasers," at Lake Garda, Italy, 1997.

20 P.Emma and R.Brinkmann, "Emittance Dilution Through Coherent Energy Spread Generation in Bending Systems," in *Proceedings of the 1997 Particle Accelerator Conference (PAC97),* Vancouver, B.C, Canada, *SLAC-PUB-7554*. May 12-16, 1997.

21 R.Bonifacio, C.Pellegrini, and L.Narducci, "Collective instabilities and high gain regime in a free electron laser," *Opt. Commun*., **50**(6), 1985.

22 J.Murphy and C.Pellegrini, "Generation of high intensity coherent radiation in the soft x-ray and VUV regions," *J. Opt. Soc. Am. B2,* **259**, 1985.

23 R. Bonifacio *et. al.*, "Spectrum, Temporal Structure, and Fluctuations in a High-Gain Free-Electron Laser Starting from Noise," *Phys. Rev. Lett.*, **73**(1), p.70, 1994.